



In-situ synthesis of direct solid-state Z-scheme $V_2O_5/g-C_3N_4$ heterojunctions with enhanced visible light efficiency in photocatalytic degradation of pollutants

Yuanzhi Hong^a, Yinhua Jiang^b, Changsheng Li^a, Weiqiang Fan^b, Xu Yan^c, Ming Yan^b, Weidong Shi^{b,*}

^a School of Materials Science and Engineering, Jiangsu University, Zhenjiang 212013, PR China

^b School of Chemistry and Chemical Engineering, Jiangsu University, Zhenjiang 212013, PR China

^c School of Energy and Power Engineering, Jiangsu University, Zhenjiang 212013, PR China

ARTICLE INFO

Article history:

Received 16 April 2015

Received in revised form 19 June 2015

Accepted 25 June 2015

Available online 16 July 2015

Keywords:

Z-scheme heterojunction

V_2O_5

$g-C_3N_4$

Photocatalytic activity

Visible light

ABSTRACT

The constructing of direct solid-state Z-scheme heterojunction photocatalytic system has received much attention in environmental purification and hydrogen generation from water. In this study, a novel direct solid-state Z-scheme $V_2O_5/g-C_3N_4$ heterojunctions were synthesized via a facile *in-situ* growth strategy for the first time. The photocatalytic performance was evaluated by the degradation of rhodamine B (RhB) and tetracycline (TC) under visible light irradiation ($\lambda > 420$ nm). Results show that the as-synthesized heterojunctions can significantly enhance photocatalytic activity in comparison with pure $g-C_3N_4$ and V_2O_5 . The optimum photocatalytic efficiency of VC1.0% sample for the degradation RhB was about 7.3 and 13.0 times higher than that of individual $g-C_3N_4$ and V_2O_5 , respectively. In addition, the VC1.0% sample as well as can efficiently degrade methyl orange (MO) and methylene blue (MB) under visible light. By further experimental study, the possible for the enhancing photocatalytic mechanism was found to be a direct solid-state Z-scheme heterojunction system based on the active species trapping and electron spin resonance (ESR) experiments, which not only can improve the photogenerated electron–hole pair's separation but also exhibit a strong oxidation and reduction ability for efficiency degradation of organic pollutants. This work will be useful for the design of other direct solid-state Z-scheme photocatalytic systems for application in energy conversion and environmental remediation.

© 2015 Elsevier B.V. All rights reserved.

1. Introduction

Over the past years, semiconductor photocatalysis has been considered as a promising and green technology to resolve the increasing energy and environmental crisis by using of the solar light energy, such as for pollutants degradation and hydrogen generation from water [1–5]. As is known, the photogenerated electrons and holes of the single-component photocatalyst can easily recombine each other, which results in poor quantum efficiency and low photocatalytic performance [6]. In past years, the use of heterojunction-type photocatalytic system is an important strategy to overcome this drawback because it can efficiently improve the photoexcited electron–hole separation [7–9]. Unfortunately, the disadvantage of the typical heterojunction system is that the reducibility of photogenerated electrons and the oxidiz-

ability of photogenerated holes usually become weakened after charge transfer [10]. That is to say, the high charge-separation efficiency and strong redox ability are difficult to possess at the same time. Very recently, the construction of artificial Z-scheme photocatalytic system is an ideal and effective means because it not only can reduce the bulk electron–hole recombination, but also can preserve excellent redox ability [10,11]. However, the majority of the synthesized artificial Z-scheme photocatalytic systems usually had noble metal (Ag, Ru) [12–14] or redox pair (Fe^{3+}/Fe^{2+} , IO_3^-/I^-) [15,16], which will bring about great difficulties to their practical application. Thus, it is necessary to construct a novel Z-scheme system including only two visible-light-responsive solid-state photocatalysts. More recently, the synthesis of direct solid-state Z-scheme photocatalytic system has become a research hotspot for application in environmental purification and hydrogen generation from water [17–22]. The different charge carrier transfer path of typical heterojunction and novel direct solid-state Z-scheme heterojunction are depicted in Fig. 1.

* Corresponding author. Fax: +86 511 8879 1108.
E-mail address: swd1978@ujs.edu.cn (W. Shi).

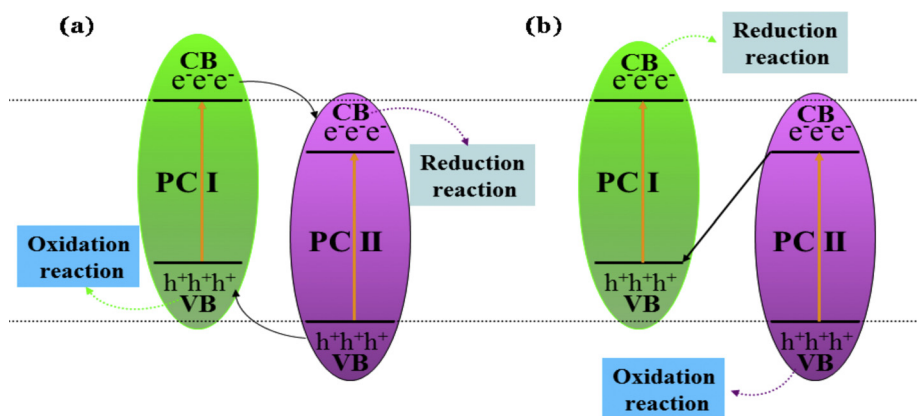


Fig. 1. Schematic illustration of the different charge carrier transfer path of (a) typical heterojunction and (b) novel direct solid-state Z-scheme heterojunction.

Graphitic carbon nitride ($g\text{-C}_3\text{N}_4$), a metal-free polymeric semiconductor, has attracted extensively attention due to its good thermal-chemical stability, electronic and optical characteristics [23]. In addition, $g\text{-C}_3\text{N}_4$ as a novel visible-light-driven photocatalyst has been reported for hydrogen evolution and pollutant degradation under visible light irradiation [24–29]. Nevertheless, the photocatalytic application of individual $g\text{-C}_3\text{N}_4$ is limited due to the rapid recombination of photogenerated electron–hole pairs, leading to the poor quantum efficiency and low photocatalytic activity. Up to now, only a few $g\text{-C}_3\text{N}_4$ -based direct Z-scheme systems have been successfully prepared for enhancing photocatalytic activity, such as $\text{TiO}_2/g\text{-C}_3\text{N}_4$ [30], $\text{BiOCl}/g\text{-C}_3\text{N}_4$ [31], $\text{Bi}_2\text{O}_3/g\text{-C}_3\text{N}_4$ [32], $\text{WO}_3/g\text{-C}_3\text{N}_4$ [33] etc. However, the TiO_2 and BiOCl can not excite in visible light because of their larger band gap ($E_g > 3.0$ eV). On the other hand, although the Bi_2O_3 and WO_3 can respond to the visible light, they only can respond visible light with the wavelength shorter than 460 nm which limit their in solar energy conversion. Therefore, it is a great challenge to construct the $g\text{-C}_3\text{N}_4$ -based direct solid-state Z-scheme system with a narrow band gap semiconductor photocatalyst for efficiently utilizing the solar light.

Vanadium pentoxide (V_2O_5), an important transition metal-oxide semiconductor, has been widely used in lithium-ion batteries, gas sensors and optoelectronic devices [34–36]. Moreover, V_2O_5 is a typical narrow band gap (~ 2.3 eV) semiconductor, which can be a good candidate for capable of capturing visible light [37,38]. What's more, V_2O_5 has suitable band edges ($ECB = 0.47$ eV, $EVB = 2.73$ eV), which can match well with $g\text{-C}_3\text{N}_4$ ($ECB = -1.2$ eV, $EVB = 1.5$ eV) to form a direct solid-state Z-scheme photocatalytic system [27,38]. If that can be accomplished, the photoexcited electron in conduction band (CB) of $g\text{-C}_3\text{N}_4$ shows the strong reducibility and the photoexcited hole on valence band (VB) of V_2O_5 exhibits the strong oxidizability, respectively.

In the present study, we have firstly prepared the direct solid-state Z-scheme $\text{V}_2\text{O}_5/g\text{-C}_3\text{N}_4$ heterojunction photocatalysts by a facile *in-situ* growth strategy. The photocatalytic performance was evaluated by the degradation of RhB and TC under visible light irradiation ($\lambda > 420$ nm). The as-synthesized Z-scheme $\text{V}_2\text{O}_5/g\text{-C}_3\text{N}_4$ photocatalysts could significantly enhance photocatalytic activity in comparison with pure $g\text{-C}_3\text{N}_4$ and V_2O_5 . In addition, the VC1.0% sample exhibited the optimum photocatalytic activity as well as possessed excellent photostability after five times cycling photocatalytic reactions. Moreover, the VC1.0% sample also can efficiently decompose other pollutant organic dyes such as methyl orange (MO) and methylene blue (MB) under visible light. Furthermore, a novel direct solid-state Z-scheme photocatalytic mechanism for the enhancing photocatalytic activity was also

proposed based on the active species trapping experiments and electron spin resonance (ESR) analysis.

2. Experimental

2.1. Materials

Melamine, NH_4VO_3 , triethanolamine (TEOA), 1,4-benzoquinone (BQ), isopropanol (IPA), and 5,5-dimethyl-1-pyrroline N-oxide (DMPO) were analytical grade agents and purchased from Aladdin (China). Rhodamine B (RhB), tetracycline (TC), methyl orange (MO) and methylene blue (MB) were analytically pure and used without further purification.

2.2. Photocatalysts preparation

The metal-free bulk $g\text{-C}_3\text{N}_4$ powders were synthesized by the thermal treatment of melamine according to the previous paper [39]. Typically, 10 g melamine was put into a 50 mL alumina crucible with a cover, then heated in a muffle furnace at a rate of $2.3^\circ\text{C}/\text{min}$ and kept for 4 h at 550°C . After being cooled to room temperature, the resulting products were collected and milled into powder in an agate mortar for further use.

The direct solid-state Z-scheme $\text{V}_2\text{O}_5/g\text{-C}_3\text{N}_4$ heterojunction photocatalysts were prepared by a facile *in-situ* growth strategy as illustrated in Fig. 2. Specifically, a certain amount of bulk $g\text{-C}_3\text{N}_4$ and different amount of NH_4VO_3 were added into an agate mortar, and grounded together. The resultant powders were transferred to a covered alumina crucible, then calcined at 500°C for 1 h with a heating rate of $5^\circ\text{C}/\text{min}$. To make clarity, the $\text{V}_2\text{O}_5/g\text{-C}_3\text{N}_4$ composites with expected V_2O_5 contents of 0, 0.5, 1.0, 1.5, 2.5 and 5.0 wt% are referred to as pure $g\text{-C}_3\text{N}_4$, VC0.5%, VC1.0%, VC1.5%, VC2.5% and VC5.0%, respectively. For comparison, bare V_2O_5 was prepared similarly but without the addition of $g\text{-C}_3\text{N}_4$.

2.3. Characterization

All of the phase compositions and crystal structures of the prepared samples were determined by powder X-ray diffraction (XRD) method using $\text{Cu K}\alpha$ radiation ($\lambda = 1.54178 \text{ \AA}$), (D/MAX-2500 diffractometer, Rigaku, Japan) with $\text{Cu-K}\alpha$ radiation source ($k = 1.54056$) over the 2θ range of $5.0\text{--}80^\circ$ at a scanning rate of $7.0^\circ \text{ min}^{-1}$. The morphology of as-prepared samples was observed by scanning electronic microscopy (SEM) on an S-4800 field emission SEM (SEM, Hitachi, Japan). The transmission electron microscopy (TEM), high-resolution TEM (HRTEM) and High angle angular dark field-scanning transmission electron microscopy (HAADF-STEM)

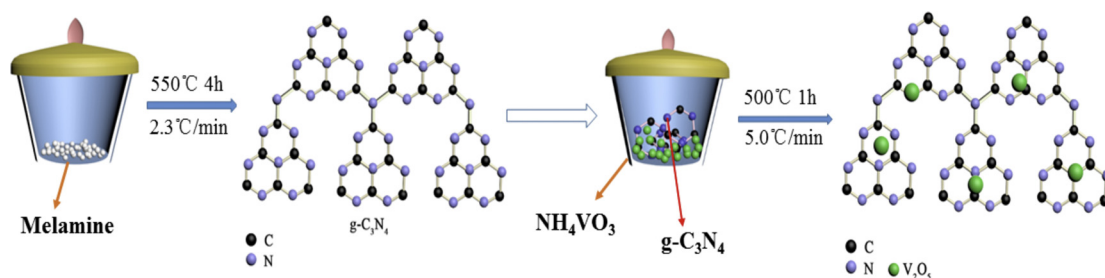


Fig. 2. Schematic illustration of the *in-situ* growth strategy of $\text{V}_2\text{O}_5/\text{g-C}_3\text{N}_4$ heterojunction photocatalysts.

were also used to characterization the sample by transmission electron microscopy (Tenai G2 F30 S-Twin, FEI) using an accelerating voltage of 200 kV. The X-ray photoelectron spectroscopy (XPS) was obtained by a Thermo ESCALAB 250X (America) electron spectrometer using 150 W Al $\text{K}\alpha$ X-ray sources. The UV–vis diffused reflectance spectra (DRS) of the samples were obtained from an UV–vis spectrophotometer (UV-2450, Shimadzu, Japan), BaSO_4 was used as a reflectance standard. The photoluminescence (PL) spectra of samples were measured on a PerkinElmer LS 55 at room temperature using a fluorescence spectrophotometer. The photocurrent measurements were performed by using a CHI 660B (Chenhua, China) electrochemical workstation with a standard three-electrode cell at room temperature. The electron spin resonance (ESR) analysis was conducted with a Bruker EPR A 300-10/12 spectrometer.

2.4. Photocatalytic experiments

The photocatalytic activities of the as-prepared samples were investigated by the degradation of RhB and TC under visible light irradiation. The photochemical reactor was illuminated using a 250 W xenon lamp with a 420 nm cutoff filter. In each test, 50 mg of as-prepared samples were added into 100 mL of 10 mg/L pollutants aqueous solution. Then the suspension was stirred in the dark for 40 min to achieve the adsorption–desorption equilibrium prior to visible light irradiation. The concentration changes of RhB and TC were monitored by measuring the UV–vis absorption of the suspensions at 15 min interval. During irradiation, 5 mL of the suspension was taken out and centrifuged (10,000 rpm, 10 min) to remove the photocatalysis before measurement. The peak absorbencies of RhB at 553 nm and TC at 357 nm were used to determine its concentration by a TU-1810 UV–vis spectrophotometer. In addition, the photocatalytic application of as-synthesized sample was further estimated by the degradation of MO and MB under visible light. The same operations were carried out except that the pollutants aqueous solution was replaced by 100 mL of 10 mg/L MO and MB aqueous solution. The concentrations of MO and MB were also determined by a TU-1810 UV–vis spectrophotometer at the wavelength of 464 and 664 nm, respectively.

2.5. Active species trapping and ESR experiments

It is well known that the holes (h^+), superoxide radical ($\text{O}_2^{\cdot-}$) and hydroxyl radicals (OH^{\cdot}) are the major reactive species for the photocatalytic oxidation. In order to investigate the main active species responsible for the photocatalytic reaction, TEOA (1 mM) [12,40], BQ (1 mM) [41,42], and IPA (1 mM) [12,43] were respectively employed as the scavengers for h^+ , $\text{O}_2^{\cdot-}$ and OH^{\cdot} . The method was similar to the former photocatalytic activity test. In addition, the ESR technique was further used to detect the presence of OH^{\cdot} and $\text{O}_2^{\cdot-}$ radicals in the photocatalytic reaction system under visible light ($\lambda > 420$ nm). The OH^{\cdot} and $\text{O}_2^{\cdot-}$ radicals usually can be trapped by the DMPO [44]. Before to determine the hydroxyl rad-

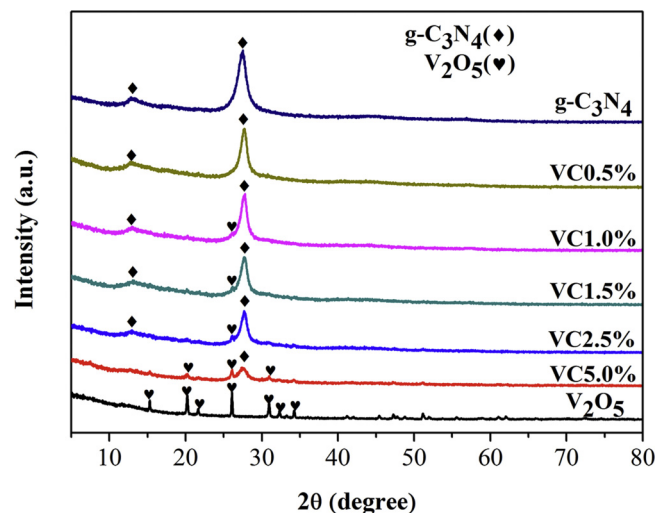


Fig. 3. XRD patterns of as-prepared photocatalysts.

icals (DMPO- OH^{\cdot}) and superoxide radicals (DMPO- $\text{O}_2^{\cdot-}$), 10.0 mg samples were dissolved in 0.5 mL deionized water (DMPO- OH^{\cdot}) or 0.5 mL methanol (DMPO- $\text{O}_2^{\cdot-}$), and then 45 μL DMPO was added with ultrasonic dispersion for 5 min, respectively.

3. Results and discussion

3.1. Characterization of as-prepared samples

The crystalline phases of the as-prepared samples were determined by XRD analysis. As shown in Fig. 3, the diffraction peaks of the pure $\text{g-C}_3\text{N}_4$ sample appears at 13.0° and 27.4° , which can be indexed to the (100) and (002) diffraction planes of graphite-like carbon nitride, respectively [41]. The bare V_2O_5 sample can be assigned to the orthorhombic phase of V_2O_5 (JCPDS 75-0457). The results reveal that as-prepared photocatalysts are well crystallized. For the $\text{V}_2\text{O}_5/\text{g-C}_3\text{N}_4$ composited samples, the characteristic peaks of $\text{g-C}_3\text{N}_4$ are gradually become weak, whereas the peak intensities of V_2O_5 become stronger with the increasing of V_2O_5 content. Moreover, no other impurity phases are discovered, indicating the as-obtained $\text{V}_2\text{O}_5/\text{g-C}_3\text{N}_4$ heterostructured photocatalysts are two-phase hybrid.

The morphologies of as-synthesized samples were characterized by SEM. From Fig. 4, we can be seen that the pure $\text{g-C}_3\text{N}_4$ was composed of different nanosizes crystals stacking layers with smooth surface. After introducing the V_2O_5 , the $\text{V}_2\text{O}_5/\text{g-C}_3\text{N}_4$ composites samples appeared some agglomeration nanoparticles on the surface of $\text{g-C}_3\text{N}_4$, resulting in the formation of a heterostructure. The morphologies, microstructures and chemical composition of the VC1.0% sample were further carried out by TEM. As shown in Fig. 5a, TEM image of VC1.0% sample shows a layered structure, which offers substrate for loading of V_2O_5 . From Fig. 5b, the HRTEM

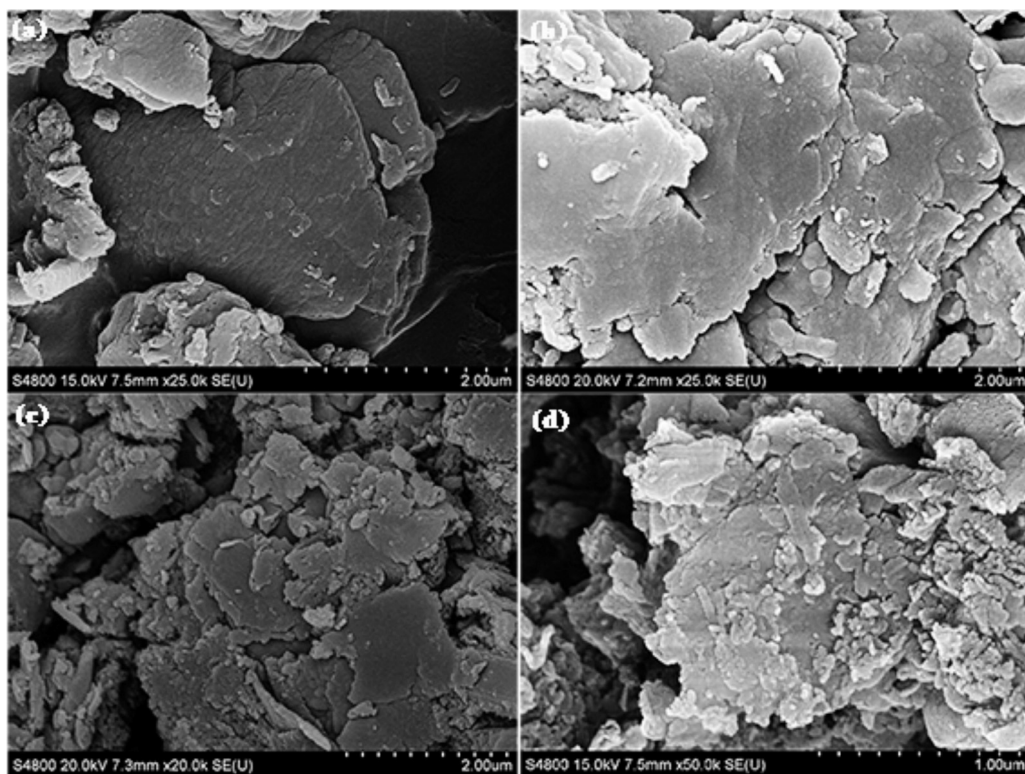


Fig. 4. SEM images of as-prepared samples (a) pure g-C₃N₄; (b) VC1.0%; (c) VC2.5%; (d) VC5.0%.

shows the lattice spaces of VC1.0% sample, which displays the lattice spaces of V₂O₅ crystallite is determined as 0.287 nm, belonging to the (400) crystal plane. However, the lattice fringe of g-C₃N₄ is difficult to be found. To further observe the combination of g-C₃N₄ and V₂O₅ in the composited VC1.0% sample, HAADF-STEM is employed. The maps of C, N, V and O are also given in Fig. 6, which illustrate that V₂O₅ is closely contacted with g-C₃N₄.

Fig. 7 shows the N₂ adsorption–desorption isotherms of as-prepared pure g-C₃N₄ and VC1.0% samples. It can be seen that the isotherms are similar and all of them are of classical type IV, suggesting the presence of mesopores. The BET surface area (S_{BET}) of the g-C₃N₄ was 13.4 m²g^{−1}, and with increasing the amount of V₂O₅, the S_{BET} of the as-prepared V₂O₅/g-C₃N₄ heterojunction photocatalysts become more and more large (from VC0.5% to VC5.0%, the

S_{BET} were found to be 162.6, 163.4, 167.3, 170.1 and 211.8 m²g^{−1}, respectively). Compared with pure g-C₃N₄, the S_{BET} of V₂O₅/g-C₃N₄ composites is increased slightly. In addition, the S_{BET} , average pore diameter and pore volume of as-prepared samples are listed in Table S1.

The surface chemical compositions and states of as-prepared pure g-C₃N₄ and VC1.0% samples were further examined by XPS. As shown in Fig. 8, in the C 1s XPS spectrum, the peak at 284.8 eV was used as the reference for calibration. The C 1s XPS spectra peaks of pure g-C₃N₄ and VC1.0% samples at 288.1 eV and 288.3 eV could be assigned to the N–C–N coordination in graphitic-like carbon nitride [45]. In the N 1s XPS spectra, the main N 1s peaks of pure g-C₃N₄ and VC1.0% samples at 398.9 eV and 398.6 eV are due to the sp²-hybridized nitrogen (C=N–C) [27]. The C 1s and N 1s

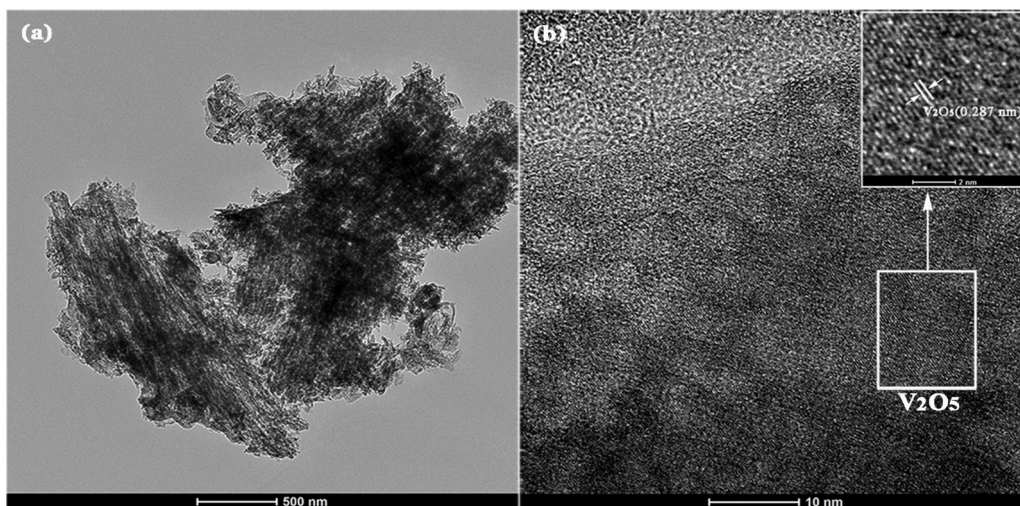


Fig. 5. (a) TEM and (b) HRTEM images of as-prepared VC1.0% sample.

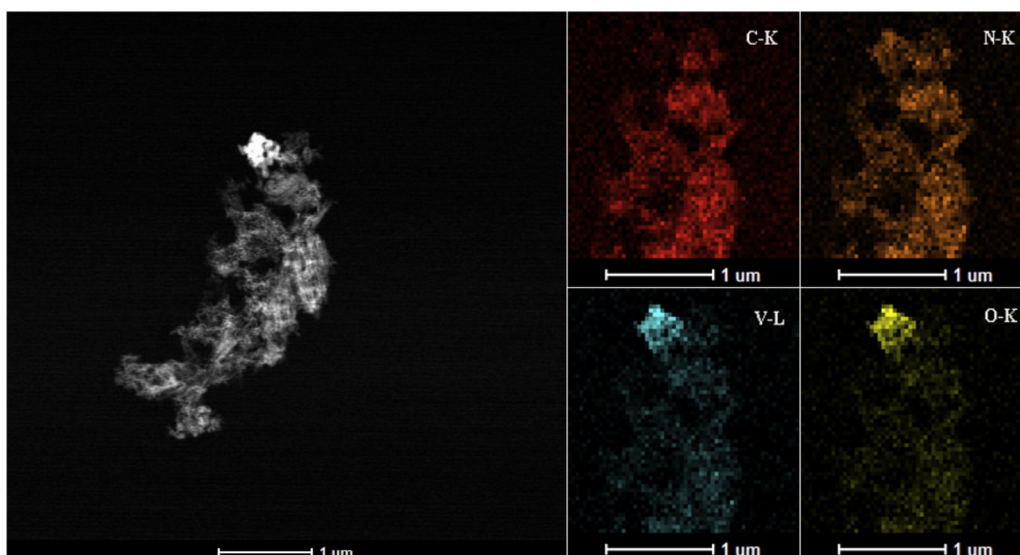


Fig. 6. HAADF-STEM images of the VC1.0% sample with maps of C–K, N–K, V–L and O–K.

binding energies change of pure $g\text{-C}_3\text{N}_4$ and VC1.0% samples may be attributed to the heterojunction interaction between $g\text{-C}_3\text{N}_4$ and V_2O_5 . In the V 2p and O 1s XPS spectrum of VC1.0% sample, the V 2p peak at 517.4 eV and 524.8 eV are ascribed to the V 2p_{3/2} and V 2p_{1/2} levels, and the O 1s peak at 532.2 eV corresponds to the V_2O_5 oxygen atom, respectively [46,47].

The UV–vis diffuse reflectance spectra of as-prepared samples are shown in Fig. 9a. As can be seen from the curve, the pure $g\text{-C}_3\text{N}_4$ shows absorption wavelengths from the ultraviolet to the visible light region up to 460 nm, and bare V_2O_5 exhibits a sharp absorption edge at about 600 nm. Compared with that of pure $g\text{-C}_3\text{N}_4$, the absorption edges of the $\text{V}_2\text{O}_5/g\text{-C}_3\text{N}_4$ heterostructured samples (VC0.5–VC5.0%) show a systematic slight red-shift. It is in good agreement with the colors change of the samples, which from light yellow turns to dark gray with increasing the V_2O_5 content (see insert picture). The results imply that all these as-synthesized photocatalysts possess visible light response. In addition, the optical band gap energy (E_g) of a semiconductor photocatalyst can be calculated by the following formula:

$$\alpha h\nu = A(h\nu - E_g)^{n/2} \quad (1)$$

where α , $h\nu$, A and E_g represent the absorption coefficient, Planck constant, light frequency, proportionality and band gap energy, respectively. The band gap energy for the $g\text{-C}_3\text{N}_4$ was determined from a plot of $(\alpha h\nu)^{1/2}$ vs. $h\nu$ ($n=4$ for indirect transition) [33],

and the V_2O_5 was obtained from a plot of $(\alpha h\nu)^2$ vs. $h\nu$ ($n=1$ for direct transition) [48]. As shown in Fig. 9b, the band gap of $g\text{-C}_3\text{N}_4$ and V_2O_5 were estimated to be 2.67 and 2.22 eV, which were nearly equal to the previous literatures [27,46]. In addition, as for other heterostructured samples (from VC0.5% to VC5.0%), the energy band gaps were found to be 2.65, 2.63, 2.60, 2.57 and 2.54 eV, respectively.

The PL analysis was used to estimate the photoinduced charge carriers separation and transfer ability of the as-prepared samples. Before the measurement, samples (10 mg) were well-dispersed 5 mL of ethanol and the PL emission spectra of the as-prepared samples monitored at an excitation wavelength of 350 nm. It is well acknowledged that the higher PL intensity indicates the fast recombination of the charge carriers, resulting in lower photocatalytic activity [49]. As shown Fig. 10a, it can be seen that pure $g\text{-C}_3\text{N}_4$ sample has a main emission peak at about 460 nm, which can be corresponded to its band gap and ascribed to the band gap recombination of electron–hole pairs [50]. After the V_2O_5 was introduced, the heterostructured samples show lower PL emission intensity compared with that of pure $g\text{-C}_3\text{N}_4$, suggesting that the recombination rate of photogenerated charge carriers become lower in $\text{V}_2\text{O}_5/g\text{-C}_3\text{N}_4$ heterojunction. Moreover, the PL intensity of the VC1.0% sample possesses the lowest PL intensity, suggesting its high photocatalytic activity. The PL result suggests that the recombination rate of electron–hole pairs can be restrained by the

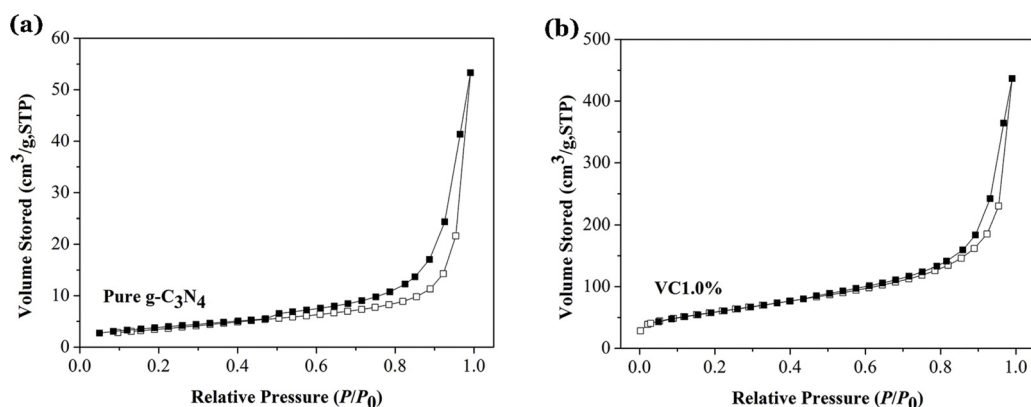


Fig. 7. N_2 adsorption–desorption isotherms of as-prepared pure $g\text{-C}_3\text{N}_4$ and VC1.0% samples (Closed symbols, desorption; open symbols, adsorption).

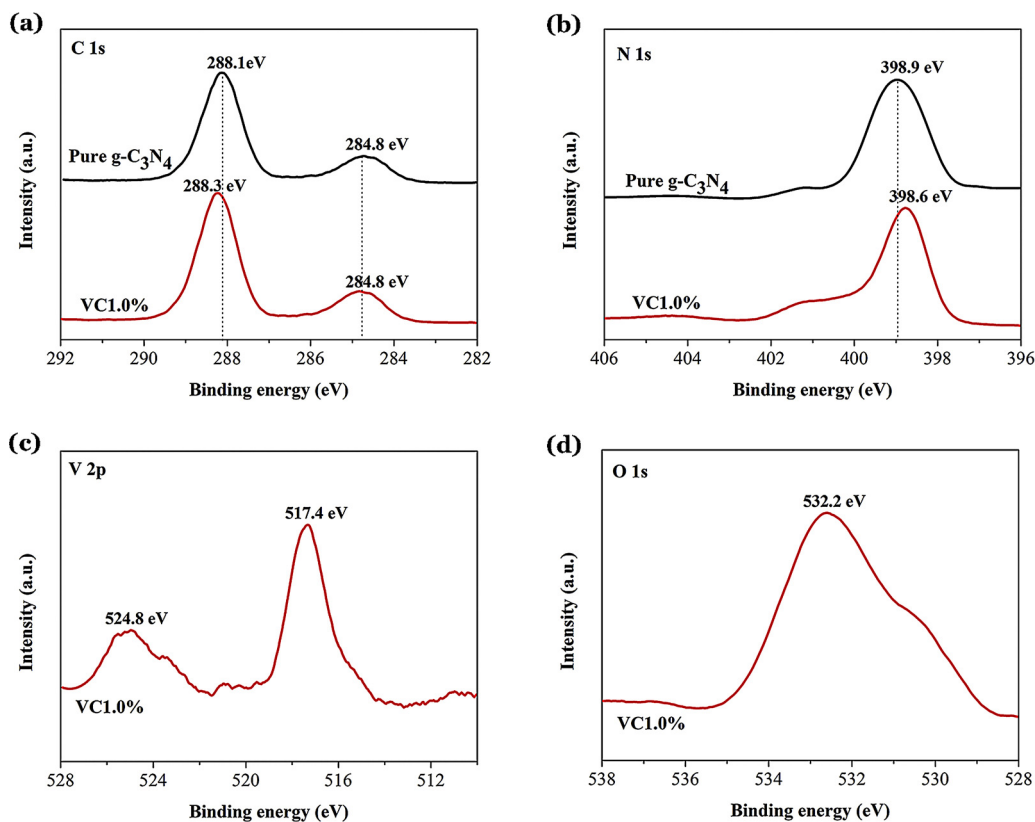


Fig. 8. XPS spectra of pure $g\text{-C}_3\text{N}_4$ and VC1.0% samples (a) C1s; (b) N1s; (c) V2p; and (d) O1s.

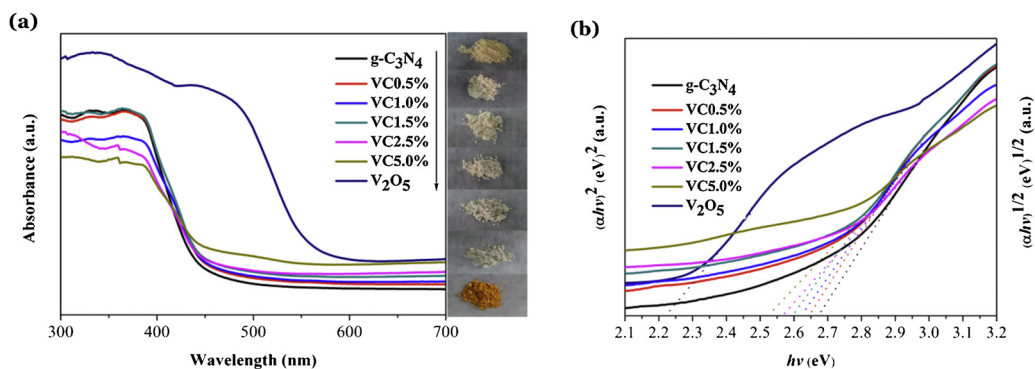


Fig. 9. (a) UV-vis diffuse reflection spectra of as-prepared photocatalysts; (b) Plots of the $(\alpha h\nu)^{1/2}$ vs. photon energy ($h\nu$) for $g\text{-C}_3\text{N}_4$ and other heterojunction samples, plots of the $(\alpha h\nu)^2$ vs. photon energy ($h\nu$) for V_2O_5 . The insert image displays the digital pictures of as-prepared samples.

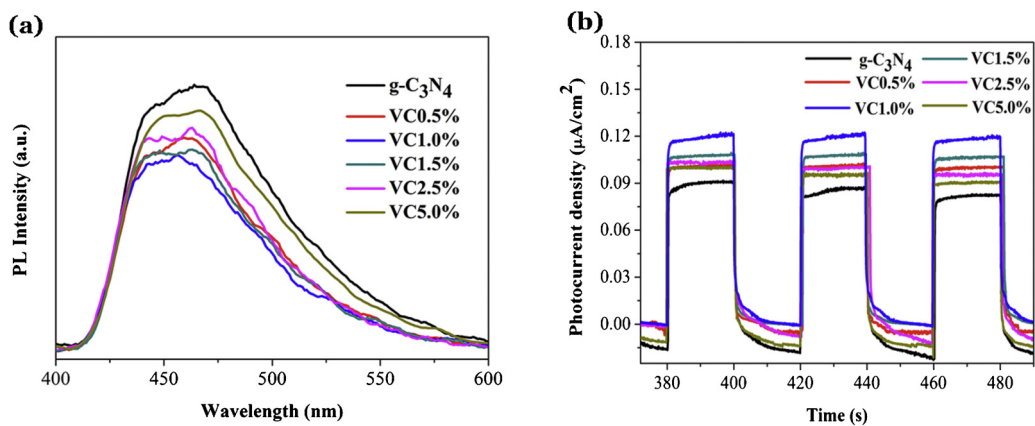


Fig. 10. (a) PL emission spectra and (b) transient photocurrent response of as-prepared samples.

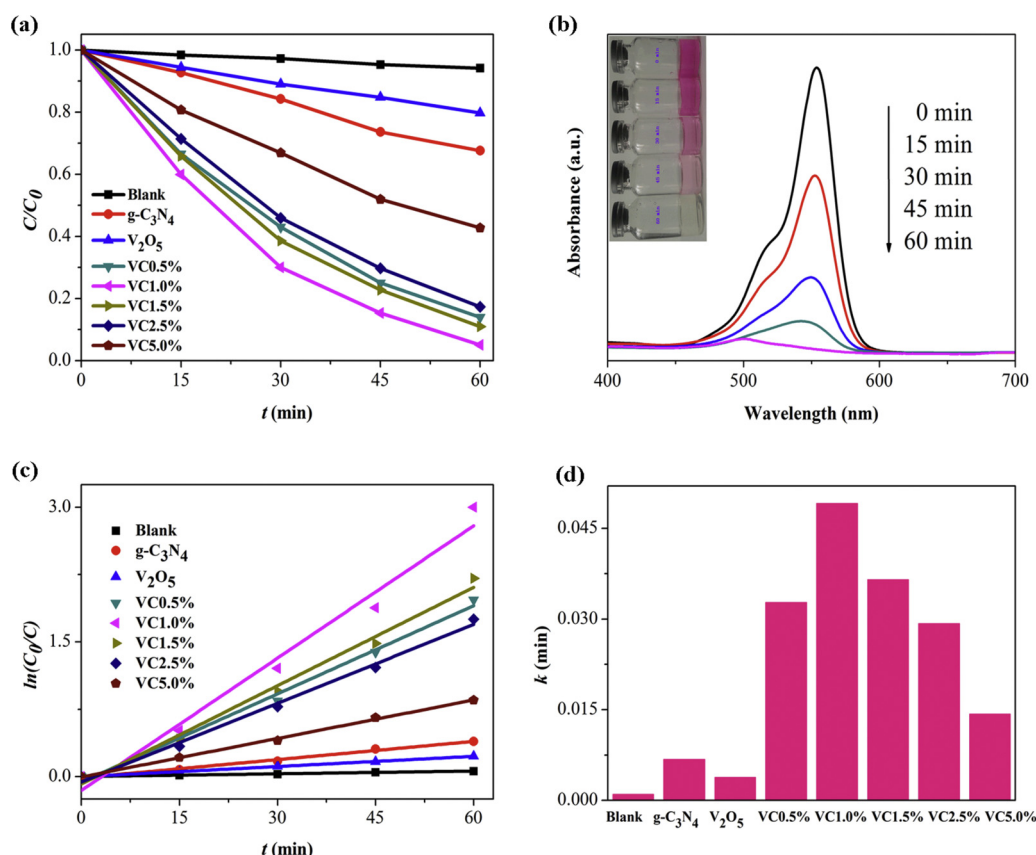


Fig. 11. (a) The photocatalytic activities of as-prepared samples for RhB degradation under visible-light ($\lambda > 420$ nm); (b) The UV-vis spectral absorption changes of RhB solution photodegraded over VC1.0% sample under visible light irradiation. The inset picture is the color change of RhB aqueous solution. (c) The pseudo-first-order reaction kinetics for RhB degradation; (d) The apparent rate constants for RhB degradation.

forming of the novel direct Z-scheme heterojunction system. In addition, the transient photocurrent responses of as-prepared samples electrodes were recorded. The photocurrents were performed for a 500 s period in an on-and-off cycle mode under visible light. From Fig. 10b, it can be seen that pure $g-C_3N_4$ shows the lower photocurrent intensity than that of other heterostructured samples. In addition, the VC1.0% sample as well as exhibits the highest photocurrent intensity in comparison with other samples. It is believed that the stronger photocurrent intensity reveals the higher electrons and holes separation efficiency [51]. Therefore, the result demonstrates that constructing of direct Z-scheme $V_2O_5/g-C_3N_4$ heterojunctions can improve the photogenerated electron-hole pair's separation.

3.2. Photocatalytic activity

It is well known that the adsorption property of catalyst is one of the crucial factors to affect the photocatalytic activity. Fig. S1 shows the photocatalysts adsorption behaviours over RhB in darkness. It can be seen that the concentration of RhB could reach adsorption-desorption equilibrium after dark reaction for 40 min. In addition, with increasing the V_2O_5 content, the as-prepared $V_2O_5/g-C_3N_4$ heterojunction photocatalysts exhibit gradually stronger adsorption properties in compared with that of pure $g-C_3N_4$. Moreover, the larger S_{BET} of $V_2O_5/g-C_3N_4$ heterojunction samples as well as can facilitate to adsorb more RhB molecules, which are benefit for improving their visible light activities.

The photocatalytic activities of the as-prepared samples were firstly evaluated by the degradation of RhB as a model pollutant under visible light irradiation ($\lambda > 420$ nm). As shown in Fig. 11a, the blank test without the catalyst reveals that the photolysis of RhB

molecule is very slowly which can be negligible. Fig. 10a indicates that the pure $g-C_3N_4$ (33.4%) and bare V_2O_5 (21.3%) samples exhibit low photocatalytic performance for degradation of RhB under visible light. However, the as-synthesized $V_2O_5/g-C_3N_4$ heterojunction photocatalysts can efficiently enhance the photocatalytic activity in compared with the individual $g-C_3N_4$ and V_2O_5 . The result illustrates that the V_2O_5 content has a significant influence on the photocatalytic activities of $V_2O_5/g-C_3N_4$ heterostructured photocatalysts. When the V_2O_5 content is increased beyond 1.0 wt%, a decrease in the photocatalytic activity was observed. Among them, the VC1.0% heterostructure shows the highest photocatalytic performance (95.5%) compared with the other samples. In addition, Fig. 11b displays the UV-vis spectral absorption changes of RhB solution photodegraded over VC1.0% sample as a function of time. Obviously, the main absorption peak of RhB molecule located at 553 nm, which decreased rapidly with extension of the exposure time. The results further demonstrate that the RhB molecules are completely degraded after 60 min visible light irradiation, which is corresponding with the color change of RhB aqueous solution.

The kinetic behaviors of as-prepared samples for photodegradation of RhB were investigated further. As illustrated in Fig. 11c, all of them fit well with the pseudo-first order correlation:

$$\ln \frac{C_0}{C} = kt \quad (2)$$

where C is the concentration of RhB remaining in the solution at irradiation time of t , C_0 is the initial concentration at $t = 0$, and k is the degradation apparent rate constant. The k values of different samples are shown in Fig. 11d, it can be found that when the V_2O_5 content is below 1.0 wt%, the photocatalytic activity increased with the increasing of V_2O_5 content. However, when the V_2O_5 content

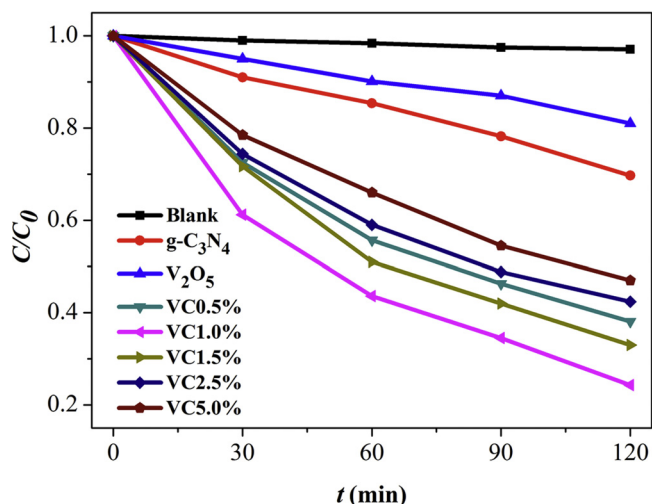


Fig. 12. The photocatalytic activities of as-prepared samples for the degradation of TC under visible light irradiation.

exceeds 1.0 wt%, the photocatalytic activity of V₂O₅/g-C₃N₄ heterostructured photocatalysts decreased as the increasing of V₂O₅ content. The optimal loading amount of V₂O₅ on g-C₃N₄ is 1.0 wt% according to its photocatalytic activity. The *k* value for RhB degradation over VC1.0% (0.0491 min⁻¹) sample is about 7.3 times higher than that of pure g-C₃N₄ (0.00677 min⁻¹), and 13.0 times than that of bare V₂O₅ (0.00379 min⁻¹). In addition, the apparent quantum efficiency of VC1.0% sample was studied by using a CEL-LED100 light with $\lambda = 420$ nm. The result was found equal to 0.07% (see Supporting information). Thus, the as-obtained photocatalyst can efficiently enhance the photocatalytic activity for degradation of RhB under visible light irradiation.

The photocatalytic activities of the as-prepared samples were further studied by the degradation of TC under visible light for evaluating the photocatalytic activity of materials and eliminating the indirect dye photosensitization in the photocatalytic system. As shown in Fig. 12, the blank test without the photocatalyst shows that the photolysis of the colorless TC molecule is very slowly which indicating that the TC molecule is very stable in the aqueous solution. Moreover, pure g-C₃N₄ (30.3%) and bare V₂O₅ (19.0%) samples exhibit low photocatalytic performance for degradation of TC under visible light. However, the as-synthesized photocatalysts can also efficiently enhance the photocatalytic activity in compared with the individual g-C₃N₄ and V₂O₅, in which is similar to the result of

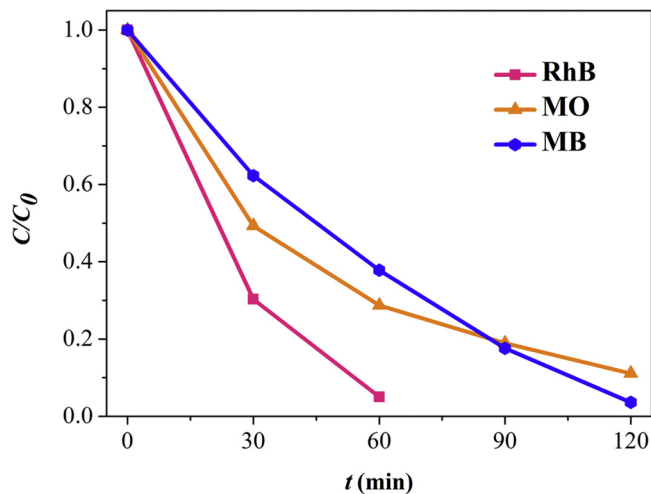


Fig. 14. The photodegradation performance of VC1.0% photocatalyst for RhB, MO, and MB degradation under visible light irradiation.

the degradation of RhB. In addition, the VC1.0% sample as well as shows the highest photocatalytic performance (75.7%) in compared with the other samples. Therefore, these results suggest that our photocatalyst display excellent visible-light-driven photocatalytic activity and can be a good candidate for application in environmental purification.

The stability of the as-synthesized VC1.0% sample was evaluated by the circulation experiments. After each cycling test, the sample was collected and washed with distilled water and absolute ethanol for three times, then the as-obtained sample were dried in vacuum at 80 °C for 12 h for next cycling reused. From Fig. 13a, it can be observed that the photocatalytic activity of the VC1.0% sample has no apparent deactivation (90.6%) even after five successive recycles for the degradation of RhB under visible light irradiation, which reveals that our photocatalyst possess high stability for its practical application. Moreover, the XRD pattern of the VC1.0% sample after 5th run cycle has been researched (Fig. 13b). It can be clearly observed that the phase and structure of the VC1.0% sample remained unchanged, which suggests that the sample is stable even after the 5th run cycle photocatalytic degradation processes. In addition, in order to further investigate the photocatalytic application of the as-prepared sample, the photocatalytic performance of the VC1.0% sample was also studied by the degradation of MO and MB under visible light. As shown in Fig. 14, the prepared sam-

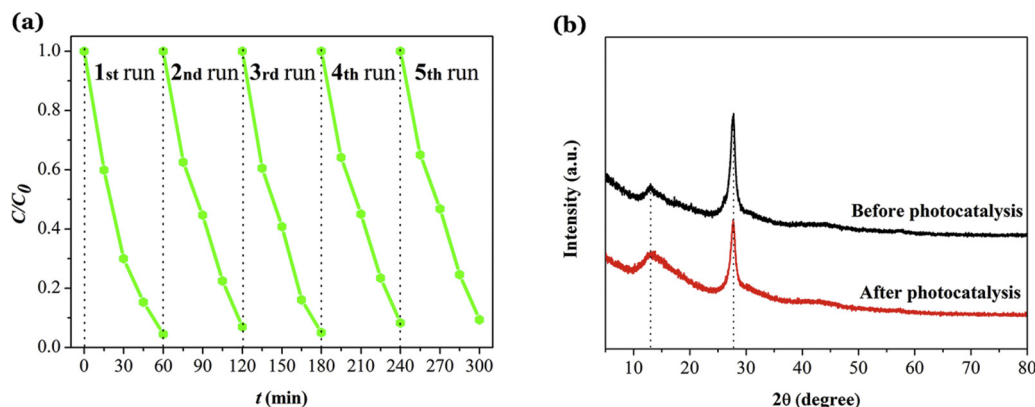


Fig. 13. (a) The repeated photocatalytic experiments of VC1.0% photocatalyst for degradation of RhB under visible light irradiation; (b) The XRD pattern of the VC1.0% sample after 5th run cycle photocatalytic experiments.

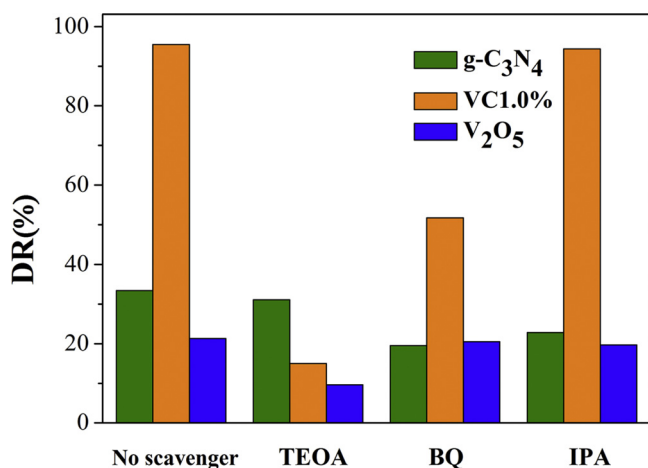


Fig. 15. The species trapping experiments for degradation of RhB over pure g-C₃N₄, V₂O₅ and VC1.0% photocatalysts under visible light irradiation.

ple also can efficiently decompose the other colored organic dyes (MO and MB) under visible light.

3.3. Photocatalytic mechanism

The different active species trapping experiments for the degradation of RhB over the pure g-C₃N₄, V₂O₅ and VC1.0% samples were first carried out to explore the enhancing photocatalytic mechanism. As shown in Fig. 15, for pure g-C₃N₄ (33.4%), when the TEOA was added into reaction solution, the photocatalytic degradation rate is almost invariable (31.1%). However, when the BQ and IPA were added into reaction solution, the degradation rate of RhB inhibited (19.5% and 22.8%), respectively. Thus, the •O₂[−] and •OH radicals are the major reactive species in the pure g-C₃N₄ reaction system. On the contrary, for bare V₂O₅ (21.3%), when the TEOA was added into reaction solution, the photocatalytic degradation rate is almost inhibited (9.6%). When the BQ and IPA were added, the degradation rate of RhB almost no changed (20.5% and 19.7%), implying that the h⁺ is the major reactive species in the pure V₂O₅ reaction system. On the other hand, for the VC1.0% sample (95.5%), it can be seen that when TEOA was added, the photocatalytic degradation rate is decreased significantly (15.0%), indicating the h⁺ is the predominant active species. When the BQ was added into reaction solution, the degradation rate of RhB also inhibited slightly (51.7%), suggesting the •O₂[−] also plays an important role in the photocatalytic process. To our surprise, when the IPA was added into reaction solution, the photocatalytic degradation rate is not obviously changed (94.4%), indicating that the •OH does not contribute to the degradation of RhB. Therefore, the h⁺ and •O₂[−] radicals are the major reactive species in the VC1.0% reaction system.

The ESR technique was further used to detect the presence of •OH and •O₂[−] radicals in the pure V₂O₅, g-C₃N₄ and VC1.0% photocatalytic reaction systems under visible light. As shown in Fig. 16, for pure g-C₃N₄ and VC1.0% samples, the four characteristic peaks of the DMPO-•OH adducts (Fig. 16a) and six characteristic peaks of DMPO-•O₂[−] adducts (Fig. 16b) are observed, indicating that the •OH and •O₂[−] radicals produced in both g-C₃N₄ and VC1.0% reaction systems. However, for bare V₂O₅ sample, there are no the characteristic peaks of DMPO-•OH adducts or the characteristic peaks of DMPO-•O₂[−] adducts are observed, implying that no •OH or •O₂[−] radicals generated in V₂O₅ reaction system. Moreover, compared with pure g-C₃N₄ and VC1.0% samples, the •O₂[−] and •OH signals intensities of VC1.0% sample is obviously stronger than that of pure g-C₃N₄, suggesting that the amount of •O₂[−] and •OH radicals generated on the VC1.0% heterostructured surface is more than that

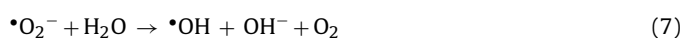
of pure g-C₃N₄. Therefore, according to the above results of the active species trapping experiments and this ESR analysis, it can be inferred that the •O₂[−] played a major role in the g-C₃N₄ and VC1.0% photocatalytic reactions rather than the •OH.

In order to explain the enhanced photocatalytic activity mechanism, the band edge positions of the valence band (VB) and conduction band (CB) potentials of g-C₃N₄ and V₂O₅ were confirmed. For a semiconductor, the VB and CB can be calculated according to the empirical equation:

$$E_{CB} = X - E^e - \frac{1}{2}E_g \quad (3)$$

$$E_{VB} = E_{CB} + E_g \quad (4)$$

The X values for g-C₃N₄ and V₂O₅ are 4.73 and 6.10 eV, respectively [33,52]. E^e is the energy of free electrons on the hydrogen scale (E^e = 4.5 eV), and E_g is the band gap energy of the semiconductor (E_g for g-C₃N₄, V₂O₅ are 2.67 and 2.22 eV, respectively). From the calculation, the ECB of g-C₃N₄ and V₂O₅ are about −1.10 and 0.49 V vs. NHE, and the EVB of g-C₃N₄ and V₂O₅ are estimated to be 1.57 and 2.71 V vs. NHE, respectively. Thus, for the pure g-C₃N₄, the photogenerated electrons on the CB of g-C₃N₄ can react with O₂ to form •O₂[−] radicals due to the position of CB of g-C₃N₄ is more negative than the potential of O₂/•O₂[−] (−0.33 V vs. NHE) [53]. Whereas, the VB potential of g-C₃N₄ is lower than the standard redox potential of •OH, H⁺/H₂O (2.72 V vs. NHE) [54], implies that the photoexcited holes in the VB of g-C₃N₄ cannot oxidize the adsorbed H₂O molecules to product •OH. However, the results of active species trapping and ESR analysis demonstrated that the •OH can be produced in the g-C₃N₄ photocatalytic system. Therefore, the •OH may be generated by further reduction of •O₂[−], which is an indirect way to form the •OH [32,55]:



As for bare V₂O₅, the photogenerated electrons on the CB of V₂O₅ cannot react with O₂ to form •O₂[−] radicals because the position of CB of V₂O₅ is less negative than the potential of O₂/•O₂[−] (−0.33 V vs. NHE). The VB potential of V₂O₅ is lower than the standard redox potential of •OH, H⁺/H₂O (2.72 V vs. NHE), suggests that the photoexcited holes in the VB of V₂O₅ also cannot oxidize the adsorbed H₂O molecules to product •OH. It is corresponding with the active species trapping experiments and ESR analysis that no •OH or •O₂[−] radicals produced in V₂O₅ system.

On the basis of the above experimental results, a novel direct solid-state Z-scheme mechanism for the enhanced photocatalytic activity of V₂O₅/g-C₃N₄ heterojunctions was proposed. As illustrated in Fig. 17, both g-C₃N₄ and V₂O₅ can be initiated by the visible-light to yield photogenerated electron-hole pairs. If the charge transfer path of photogenerated electron-hole pairs is like the typical heterojunction system, then the photogenerated electrons in the CB of V₂O₅ will product fewer •O₂[−] radicals because of its low reducibility. Thus, the photogenerated electrons in the CB of V₂O₅ tend to transfer and recombine with the photogenerated holes in the VB of g-C₃N₄. In this way, the more photogenerated electrons accumulated in the CB of g-C₃N₄ can reduce the adsorbed O₂ to form more •O₂[−], which is a powerful oxidative specie can break down the chromophores of organic pollutants into small molecules, e.g., CO₂ and H₂O [56]. Meanwhile, the photogenerated holes left behind in the VB of V₂O₅ can directly oxidize organic pollutants. Therefore, it can draw a conclusion that the photocatalytic reaction of prepared V₂O₅/g-C₃N₄ heterojunctions followed a direct solid-state Z-scheme mechanism, which could improve

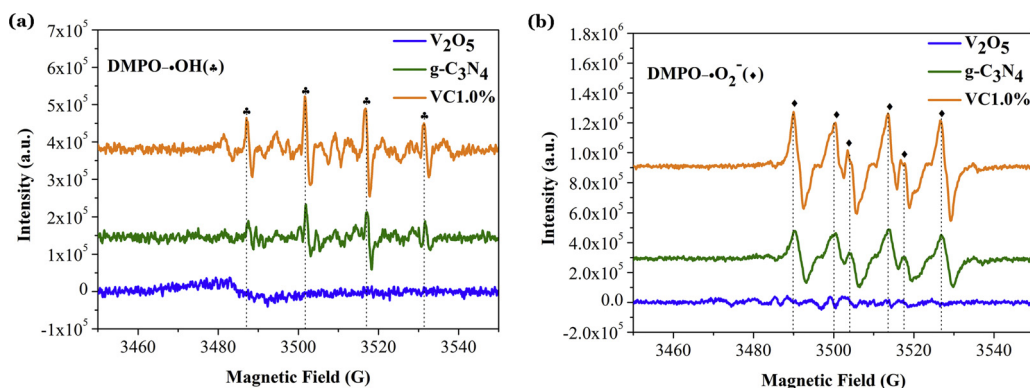


Fig. 16. DMPO spin-trapping ESR spectra in aqueous dispersion of V_2O_5 , $g-C_3N_4$, and VC1.0% samples for (a) $DMPO-•OH$ and (b) $DMPO-•O_2^-$ irradiated for 60 s.

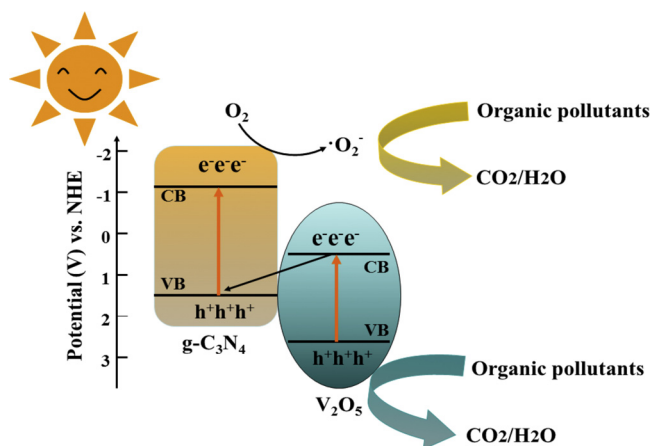


Fig. 17. The possible photocatalytic mechanism of $V_2O_5/g-C_3N_4$ heterojunction photocatalysts for degradation of organic pollutants under visible light irradiation.

the photogenerated electron–hole pair’s separation and transfer as well as show a strong oxidation and reduction ability for efficiency degradation of organic pollutants.

4. Conclusions

In summary, we have firstly constructed the novel direct solid-state Z-scheme $V_2O_5/g-C_3N_4$ heterojunction photocatalysts by a facile *in-situ* growth strategy. The as-prepared photocatalysts could be widely used for environmental purification of organic pollutants in aqueous solution because of its highly efficient and stable visible-light-driven photocatalytic performance. In addition, the enhancing photocatalytic activity was due to the formation of a direct solid-state Z-scheme heterojunction between the $g-C_3N_4$ and V_2O_5 , which resulting in the electrons in the CB of $g-C_3N_4$ exhibits high reducibility and the holes in the VB of V_2O_5 shows high oxidizability. Moreover, it should be pointed out that our photocatalysts are cost saving, high efficiency, good recyclable and easy for large-scale production.

Acknowledgements

The authors are grateful for the National Natural Science Foundation of China (21276116, 21477050, 21301076 and 21303074), Excellent Youth Foundation of Jiangsu Scientific Committee (BK20140011), Chinese–German Cooperation Research Project (GZ1091), Program for High-Level Innovative and Entrepreneurial Talents in Jiangsu Province, Program for New Century Excellent Talents in University (NCET-13-0835), Henry Fok Education Foun-

dation (141068) and Six Talents Peak Project in Jiangsu Province (XCL-025).

Appendix A. Supplementary data

Supplementary data associated with this article can be found, in the online version, at <http://dx.doi.org/10.1016/j.apcatb.2015.06.057>

References

- [1] Z.G. Zou, J.H. Ye, K. Sayama, H. Arakawa, *Nature* 414 (2001) 625–627.
- [2] R. Asahi, T. Morikawa, K. Aoki, Y. Taga, *Science* 293 (2001) 269–271.
- [3] M.N. Chong, B. Jin, C.W. Chow, C. Saint, *Water Res.* 44 (2010) 2997–3027.
- [4] C.C. Chen, W.H. Ma, J.C. Zhao, *Chem. Soc. Rev.* 39 (2010) 4206–4219.
- [5] A. Kubacka, M. Fernandez-Garcia, G. Colon, *Chem. Rev.* 112 (2012) 1555–1614.
- [6] F.L. Formai, S.R. Pendlebury, M. Cornuz, S.D. Tilley, M. Gratzel, T.R. Durrant, *J. Am. Chem. Soc.* 136 (2014) 2564–2574.
- [7] M. Ge, Y.F. Li, L. Liu, Z. Zhou, W. Chen, *J. Phys. Chem. C* 115 (2011) 5220–5225.
- [8] Y. Hou, F. Zuo, A. Dagg, P.Y. Feng, *Nano Lett.* 12 (2012) 6464–6473.
- [9] Y.J. Wang, Q.S. Wang, X.Y. Zhan, F.M. Wang, M. Safdar, J. He, *Nanoscale* 5 (2013) 8326–8339.
- [10] P. Zhou, J.G. Yu, M. Jaroniec, *Adv. Mater.* 26 (2014) 4920–4935.
- [11] H.J. Yun, H. Lee, N.D. Kim, D.M. Lee, S.J. Yu, J. Yi, *ACS Nano* 5 (2011) 4048–4090.
- [12] X.F. Wang, S.F. Li, Y.Q. Ma, H.G. Yu, J.G. Yu, *J. Phys. Chem. C* 115 (2011) 14648–14655.
- [13] L.Q. Ye, J.Y. Liu, C.Q. Gong, L.H. Tian, T.Y. Peng, L. Zan, *ACS Catal.* 2 (2012) 1677–1683.
- [14] Y. Sasaki, H. Kato, A. Kudo, *J. Am. Chem. Soc.* 135 (2013) 5441–5449.
- [15] K. Maeda, D.L. Lu, K. Domen, *ACS Catal.* 3 (2013) 1026–1033.
- [16] Y. Sasaki, A. Iwase, H. Kato, A. Kudo, *J. Catal.* 259 (2008) 133–137.
- [17] S.F. Chen, L. Ji, W.M. Tang, X.L. Fu, *Dalton Trans.* 42 (2013) 10759–10768.
- [18] S.F. Chen, Y.F. Hu, L. Ji, X.L. Jiang, X.L. Fu, *Appl. Surf. Sci.* 292 (2014) 357–366.
- [19] D.F. Xu, B. Cheng, S.W. Cao, J.G. Yu, *Appl. Catal. B: Environ.* 164 (2015) 380–388.
- [20] X.W. Wang, G. Liu, Z.G. Chen, F. Li, L.Z. Wang, G.Q. Lu, H.M. Cheng, *Chem. Commun.* (2009) 3452–3454.
- [21] F.Y. Xu, W. Xiao, B. Cheng, J.G. Yu, *Int. J. Hydrogen Energy* 39 (2014) 15394–15402.
- [22] L.J. Zhang, S. Li, B.K. Liu, D.J. Wang, T.F. Xie, *ACS Catal.* 4 (2014) 3724–3729.
- [23] J.M. Hu, W.D. Cheng, S.P. Huang, D.S. Wu, Z. Xie, *Appl. Phys. Lett.* 89 (2006) 261117.
- [24] X. Wang, K. Maeda, A. Thomas, K. Takanabe, G. Xin, J.M. Carlsson, K. Domen, M. Antonietti, *Nat. Mater.* 8 (2009) 76–80.
- [25] Q.J. Xiang, J.G. Yu, M. Jaroniec, *J. Phys. Chem. C* 115 (2011) 7355–7363.
- [26] A.J. Du, S. Stefano, Z. Li, D.W. Wang, Y. Jiao, T. Liao, Q. Sun, Y.H. Ng, Z.H. Zhu, R. Amal, S.C. Smith, *J. Am. Chem. Soc.* 134 (2012) 4393–4397.
- [27] S.C. Yan, Z.S. Li, Z.G. Zou, *Langmuir* 26 (2010) 3894–3901.
- [28] T.T. Li, L.H. Zhao, Y.M. He, J. Cai, M.F. Luo, J.J. Lin, *Appl. Catal. B: Environ.* 129 (2013) 255–263.
- [29] Y.S. Jun, E.Z. Lee, X. Wang, W.H. Hong, G.D. Stucky, A. Thomas, *Adv. Funct. Mater.* 23 (2013) 3661–3667.
- [30] J.G. Yu, S.H. Wang, J.X. Low, W. Xiao, *Phys. Chem. Chem. Phys.* 15 (2013) 16883–16890.
- [31] Y. Bai, P.Q. Wang, J.Y. Liu, X.J. Liu, *RSC Adv.* 4 (2014) 19456–19461.
- [32] J.F. Zhang, Y.F. Hu, X.L. Jiang, S.F. Chen, S.G. Meng, *J. Hazard. Mater.* 280 (2014) 713–722.
- [33] S.F. Chen, Y.F. Hu, S.G. Meng, X.L. Fu, *Appl. Catal. B: Environ.* 150–151 (2014) 564–573.
- [34] A.D. Raj, T. Pazhanivel, P.S. Kumar, D. Mangalaraj, D. Nataraj, N. Ponpandian, *Curr. Appl. Phys.* 10 (2010) 531–537.

- [35] A.Z. Moshfegh, A. Ignatiev, *Thin Solid Films* 198 (1991) 251–269.
- [36] B.X. Li, Y. Xu, G.X. Rong, M. Jing, Y. Xie, *Nanotechnology* 17 (2006) 2560–2566.
- [37] R. Akbarzadeh, S.B. Umbarkar, R.S. Sonawane, *Appl. Catal. A* 374 (2010) 103–109.
- [38] J. Su, X.X. Zou, G.D. Li, X. Wei, C. Yan, Y.N. Wang, J. Zhao, L.J. Zhou, J.S. Chen, *J. Phys. Chem. C* 115 (2011) 8064–8071.
- [39] S.C. Yan, Z.S. Li, Z.G. Zou, *Langmuir* 25 (2009) 10397–10401.
- [40] J.L. Wang, Y. Yu, L.Z. Zhang, *Appl. Catal. B: Environ.* 136–137 (2013) 112–121.
- [41] Y.L. Tian, B.B. Chang, J.L. Lu, J. Fu, F.N. Xi, X.P. Dong, *ACS Appl. Mater. Interfaces* 5 (2013) 7079–7085.
- [42] Z.H. Chen, W.L. Wang, Z.G. Zhang, X.M. Fang, *J. Phys. Chem. C* 117 (2013) 19346–19352.
- [43] U.A. Joshi, J.R. Darwent, H.P. Yiu, M.J. Rosseinsky, *J. Chem. Technol. Biotechnol.* 86 (2011) 1018–1023.
- [44] X.J. Bai, L. Wang, R.L. Zong, Y.F. Zhu, *J. Phys. Chem. C* 117 (2013) 9952–9961.
- [45] X.J. Wang, W.Y. Yan, F.T. Li, Y.B. Xue, R.H. Liu, Y.J. Hao, *Ind. Eng. Chem. Res.* 52 (2013) 17140–17150.
- [46] J. Su, X.X. Zou, G.D. Li, X. Wei, C. Yan, Y.N. Wang, J. Zhao, L.J. Zhou, J.S. Chen, *J. Phys. Chem. C* 115 (2011) 8064–8071.
- [47] M. Gurnlakshmi, M. Selvaraj, A. Selvamani, P. Vijayan, N.R. Sasi-Rekha, K. Shanthi, *Appl. Catal. A* 449 (2012) 31–46.
- [48] H.Q. Jiang, M. Nagai, K. Kobayashi, *J. Alloys Compd.* 479 (2009) 821–827.
- [49] L.L. Chen, W.X. Zhang, C. Feng, Z.H. Yang, Y.M. Yang, *Ind. Eng. Chem. Res.* 51 (2012) 4208–4214.
- [50] D. Li, Z.D. Wu, C.S. Xing, D.L. Jiang, M. Chen, W.D. Shi, S.Q. Yuan, *J. Mol. Catal. A* 395 (2014) 261–268.
- [51] B.Y. Peng, S.S. Zhang, S.Y. Yang, H.J. Wang, H. Yu, S.Q. Zhang, F. Peng, *Mater. Res. Bull.* 56 (2014) 19–24.
- [52] Y. Xu, M.A. Schoonen, *Am. Miner.* 85 (2000) 543–556.
- [53] J. Kim, C.W. Lee, W. Choi, *Environ. Sci. Technol.* 44 (2010) 6849–6854.
- [54] G.T. Li, K.H. Wong, X.W. Zhang, C. Hu, J.C. Yu, R.C. Chan, *Chemosphere* 76 (2009) 1185–1191.
- [55] S.Z. Wu, K. Li, W.D. Zhang, *Appl. Catal. B: Environ.* 324 (2015) 324–331.
- [56] N. Liang, M. Wang, L. Jin, S.S. Huang, W.L. Chen, M. Xu, Q.Q. He, J.T. Zai, N.H. Fang, X.F. Qian, *ACS Appl. Mater. Interfaces* 6 (2014) 11698–11705.